nature electronics

SUPPLEMENTARY INFORMATION
https://doi.org/10.1038/s41928-018-0175-0

In the format provided by the authors and unedited.

Fully implantable optoelectronic systems for battery-free, multimodal operation in neuroscience research

Philipp Gutruf[1,2], Vaishnavi Krishnamurthi[3], Abraham Vázquez-Guardado[4,5], Zhaoqian Xie[6], Anthony Banks[7], Chun-Ju Su[1], Yeshou Xu[8], Chad R. Haney[9], Emily A. Waters[10], Irawati Kandela[11], Siddharth R. Krishnan[1], Tyler Ray[1], John P. Leshock[12], Yonggang Huang[6], Debashis Chanda[4,5] and John A. Rogers[13]*

[1]Center for Bio-Integrated Electronics at the Simpson Querrey Institute for BioNanotechnology and the Department of Materials Science and Engineering, Northwestern University, Evanston, IL, USA. [2]Department of Biomedical Engineering, Bioscience Research Laboratories, University of Arizona, Tucson, AZ, USA. [3]Functional Material and Microsystems Research Group and Micro Nano Research Facility, RMIT University, Melbourne, Victoria, Australia. [4]CREOL, The College of Optics and Photonics, University of Central Florida, Orlando, FL, USA. [5]NanoScience Technology Center, University of Central Florida, Orlando, FL, USA. [6]Department of Civil and Environmental Engineering, Mechanical Engineering, and Materials Science and Engineering, Northwestern University, Evanston, IL, USA. [7]Department of Materials Science and Engineering Frederick Seitz Materials Research Laboratory University of Illinois at Urbana-Champaign, Urbana, IL, USA. [8]Key Laboratory of C&PC Structures of the Ministry of Education, Southeast University, Nanjing, China. [9]Center for Advanced Molecular Imaging, Radiology, and Biomedical Engineering, Northwestern University, Evanston, IL, USA. [10]Center for Advanced Molecular Imaging, Northwestern University, Evanston, IL, USA. [11]Developmental Therapeutics Core, Northwestern University, Evanston, IL, USA. [12]Department of Biomedical Engineering McCormick School of Engineering and Applied Science, Northwestern University, Evanston, IL, USA. [13]Departments of Materials Science and Engineering, Biomedical Engineering, Chemistry, Neurological Surgery, Mechanical Engineering, Electrical Engineering and Computer Science Simpson Querrey Institute & Feinberg Medical School, Northwestern University, Evanston, IL, USA. *e-mail: jrogers@northwestern.edu

Supplementary Figure 1 Device Dimensions

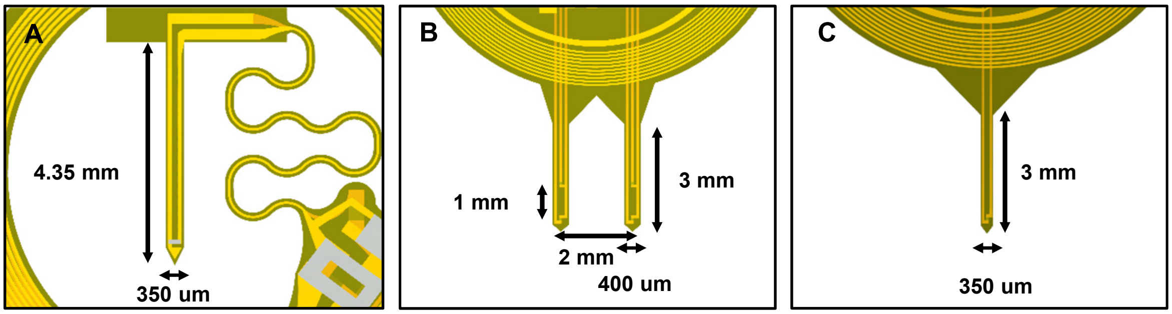

Supplementary Figure 1 (A) Injectable dimension of the regulated intensity device. (B) Schematic illustrating dimensions of the injectable of the bilateral device with multiple μ-ILED`s. (C) Injectable dimensions of the programmable intensity implant.

Supplementary Figure 2 Electrical characterization of unregulated devices

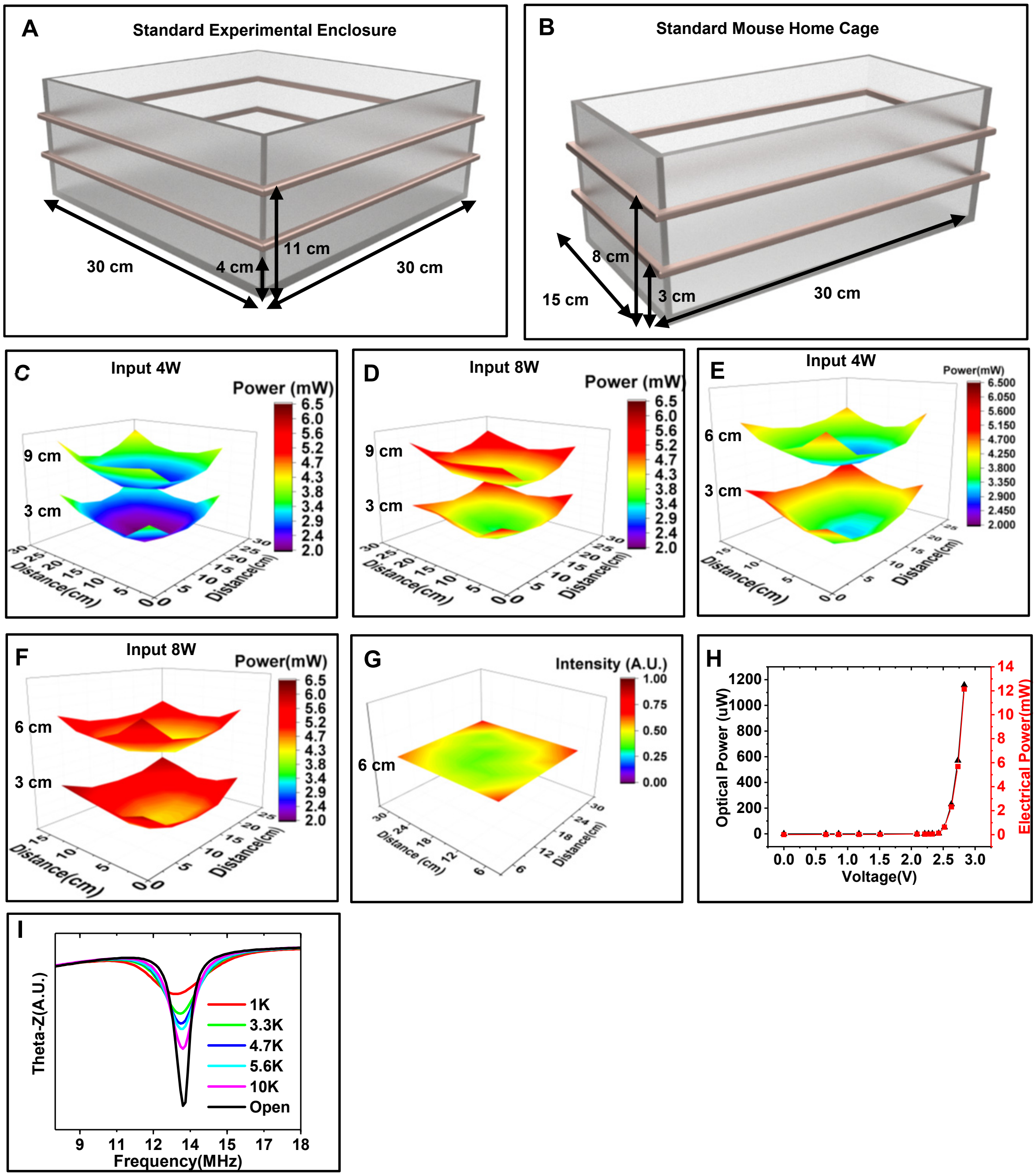

Supplementary Figure 2 (A) and (B) Antenna dimension consisting of a continuous dual loop coupled to a matching and tuning network for a standard experimental arena and a mouse homecage and respectively. (C) and (D) Rectified power in a standard experimental arena with 4 and 8W input power respectively measured with 5.6 kOhm shunt. (E) and (F) Rectified power in a standard mouse homecage with 4 and 8W input power respectively measured with 5.6 kOhm shunt. (G) Optical output of a unregulated device where the μ-ILED is directly connected to the rectifier with a 3.3 kOhm current limiting resistor. (H) Optical power VS electrical input power of the blue μ-ILED. (I) Quality factor analysis of unregulated device at increasing load

Supplementary Figure 3 Electrical characterization of devices in static and alternating RF fields

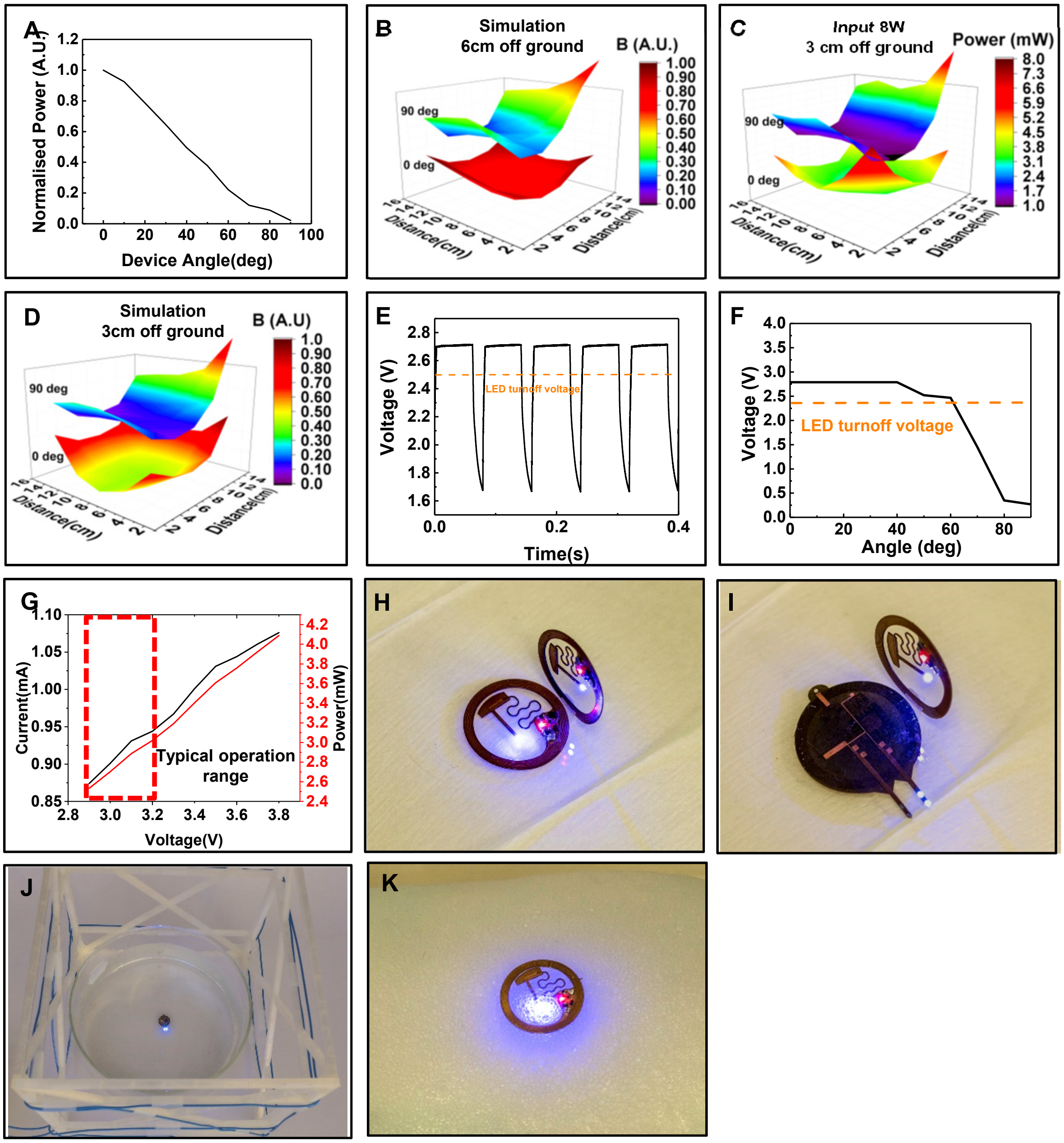

Supplementary Figure 3 (A) Unregulated rectified power at the implant with increasing angle normal to the primary antenna. (b) Simulation of rectified power at the implant for 8 W input power applied to a time multiplexed antenna across a cage (20 x 20 cm) at an implant height of 6 cm and at orientations of 0 and 90 degree with respect to ground. (c) Rectified power at the implant for 8 W input power in a time multiplexed cage (20 x 20 cm) at an implant height of 3 cm and at orientations of 0 and 90 degree with respect to ground. (d) Simulation of rectified power at the implant for 8 W input power in a time multiplexed cage (20 x 20 cm) at an implant height of 3 cm and at orientations of 0 and 90 degree with respect to ground. (E) Voltage waveform at the regulated implant demonstrating sharp ON and OFF behavior despite closed loop power voltage regulation. (F) Regulated device output voltage in a non-multiplexed cage. (G) Regulator and µController power consumption measured before the rectifier of the adjustable intensity device with increasing input voltage (low light intensity setting) (h-i) Photographic images of regulated, active devices operated with orthogonal orientations while in close proximity. (J) Photographic images of regulated devices operated in large bodies of saline solution. (K) Photographic images of a regulated device operating and floating on aqueous foam.

Supplementary Figure 4 Comparison with current Technology

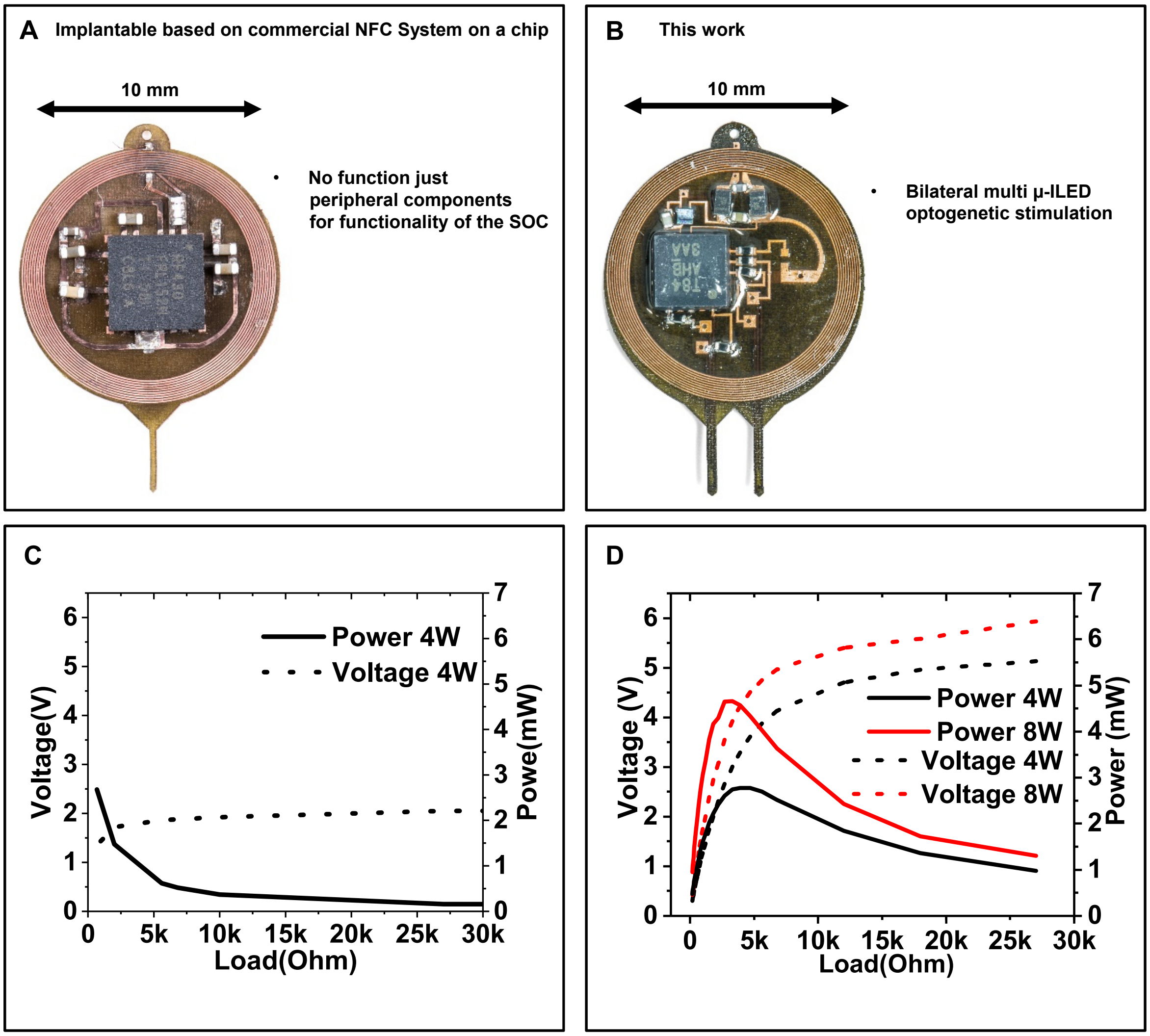

Supplementary Figure 4 (A) System demonstration of a commercially available system on a chip SOC and its application in a implantable with no function (B) The system shown in this work as a comparison (C) Power output of the SOC`s energy harvesting system (D) Power output of the energy harvesting system presented here.

Discussion

Here we demonstrate the advantages of our system towards applications in optogenetic stimulation. As demonstrated in panel (A) the footprint of commercial systems and associated components are too large to be feasible to include optogenetic stimulation. Furthermore the voltage and current provided by the energy harvesting system is insufficient to power optoelectronic components such as blue LED`s that have a turn on voltage of 2.3V

Supplementary Figure 5 Optical characterization

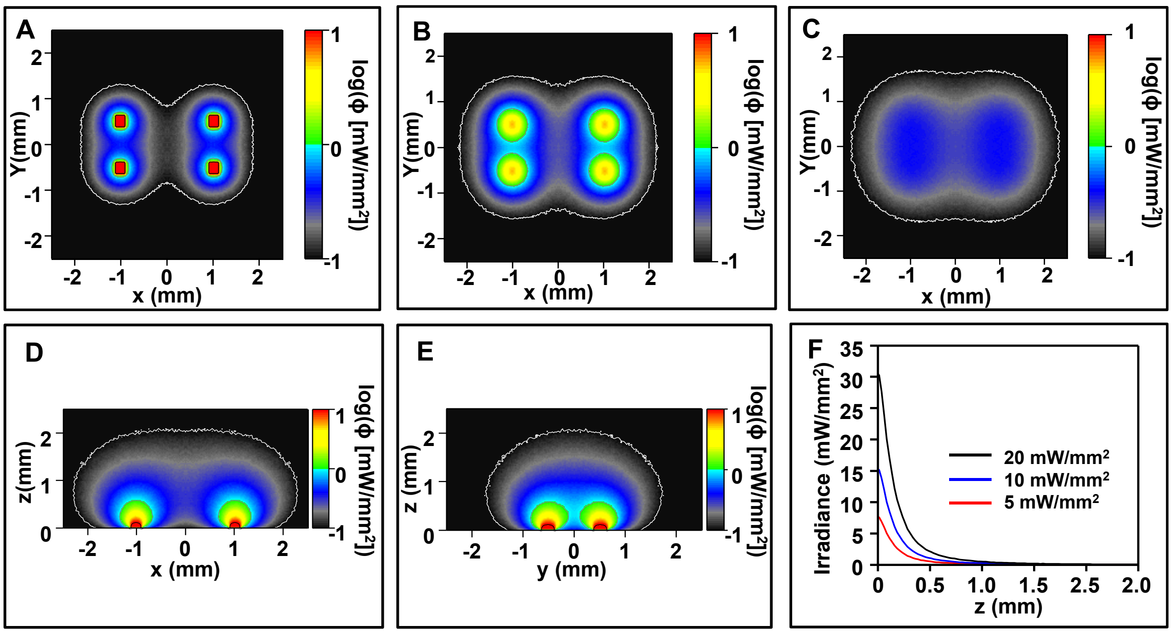

Supplementary Figure 5 Monte Carlo simulation results of the irradiance in turbid media replicating operational conditions in the brain. (A) Results 10 µm above the light source (Z axis). (B) Results 200 µm above the light source (Z axis). (C) Results 1000 µm above the light source (Z axis). (D) Cross sectional results representing the coronal orientation in the animal. (E) Cross sectional results representing the sagittal orientation in the animal. (F) Local power vs Z axis distance above the light source.

Supplementary Figure 6 Animal welfare – weight monitoring

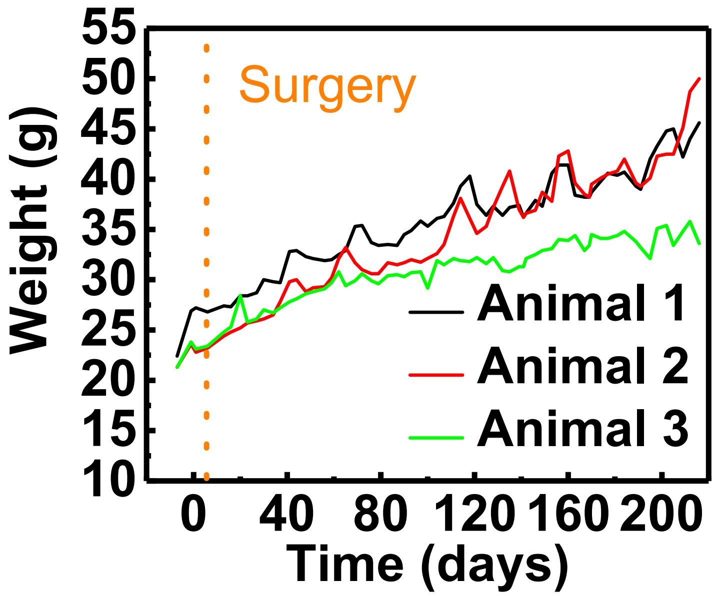

Supplementary Figure 6 Progression of the animal weight before and after implantation**.**

Supplementary Figure 7 Immunobiological Impact

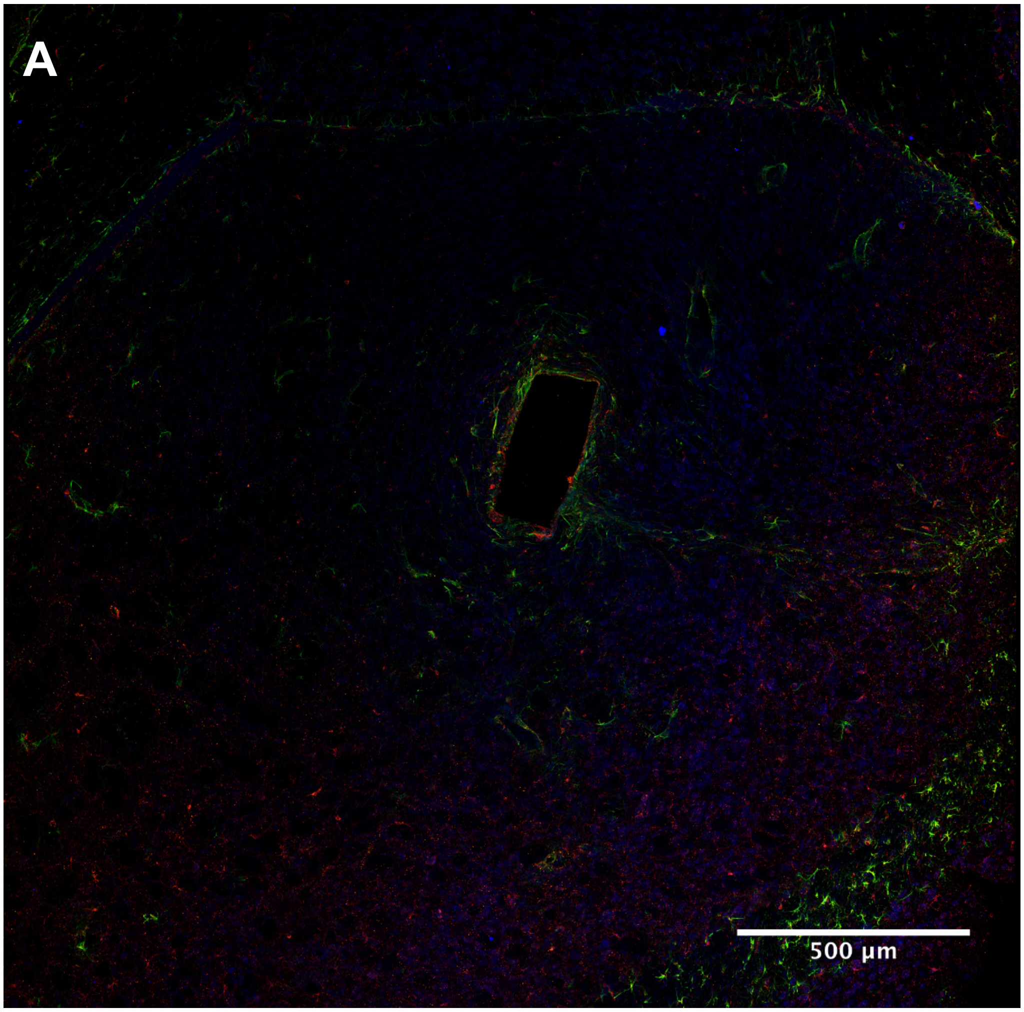

B

Antibody	Species	Dilution	Source
GFAP	Guinea Pig	1:500	Synaptic Systems
Iba1	Rabbit	1:300	Wako Chemicals
Alexa Fluor 488 anti-Rabbit IgG	Goat	1:1000	Life Technologies
Alexa Fluor 568 anti-guinea pig IgG	Goat	1:1000	Life Technologies
Neurotrace 435/455	N/A	1:100	Life Technologies

Supplementary Figure 7 (A) Immunohistochemistry results showing the immunoreactive glial response and lesions of the injectable µ-ILED on the target tissue. (B) Antibodies used in the analysis with detailed information on source and dilution.

Supplementary Figure 8 Implantation programmable intensity device

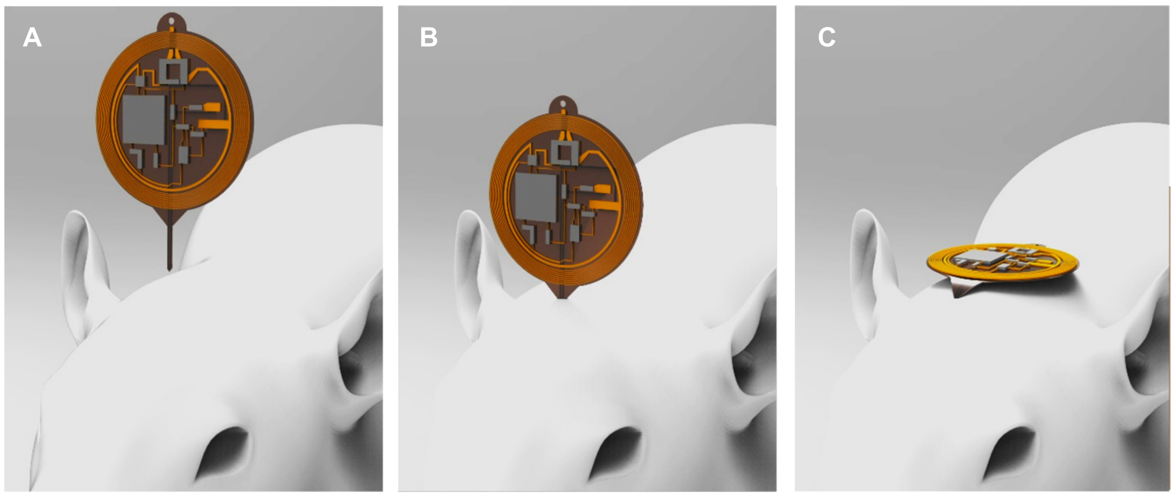

Supplementary Figure 8 Rendering of implantation procedure for the programmable intensity device. (A) Opening of the scalp, positioning and opening of the scull. (B) Insertion in target area and fixation with cyanoacrylate. (C) Bending backwards of the device with subsequent subdermal fixation by suturing the sculp over the device.

Supplementary Figure 9 Device operation in MRI

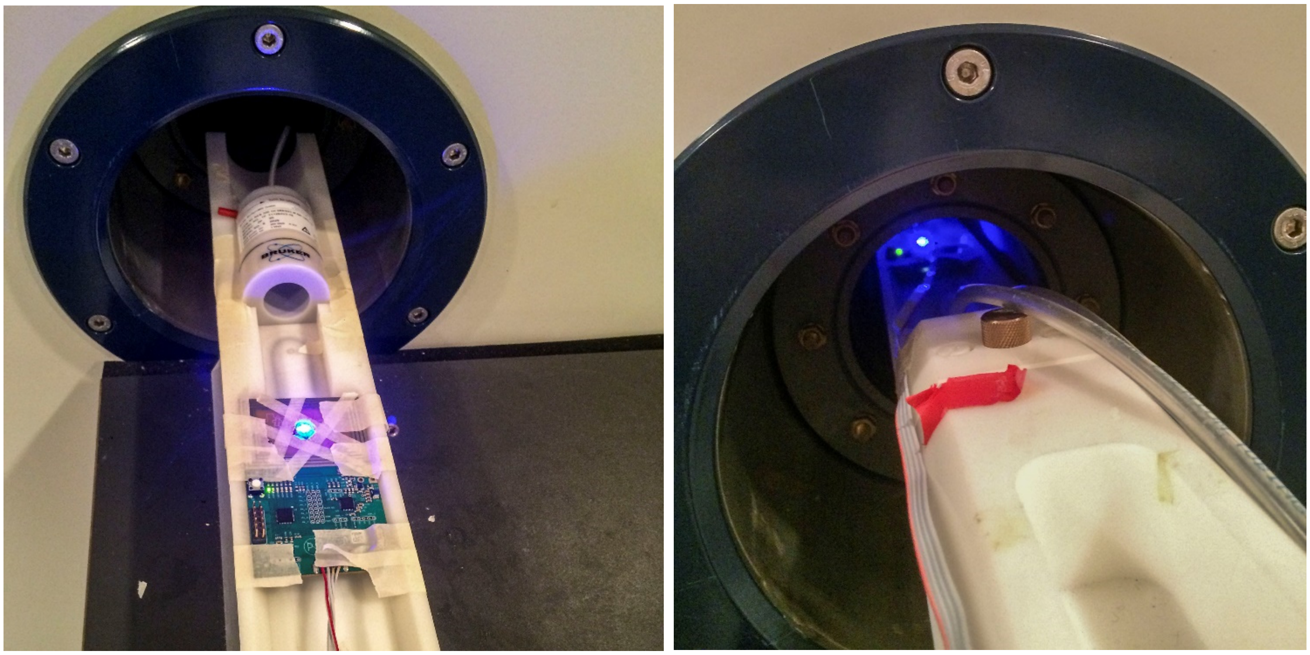

Supplementary Figure 9 Operation of implants in an MRI scanner facilitated by a primary antenna with integrated power source free of magnetic components for use in high magnetic fields. The implant is affixed in the center of the primary coil for operational tests.

Supplementary Figure 10 Thermal load measured in air

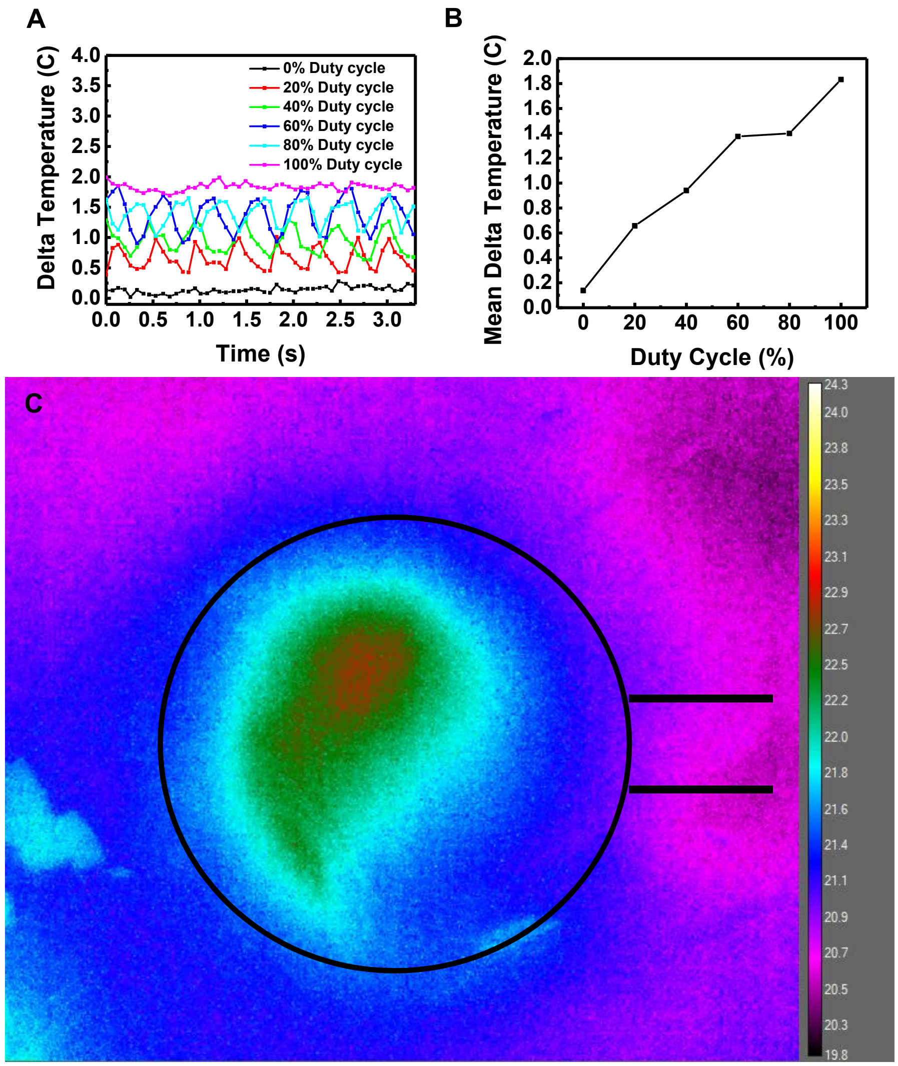

Supplementary Figure 10 (a) Temperature variation of a regulated device with electrical power around 4 mW at 2 Hz stimulation at the μ-ILEDs on the injectable in air (b) Mean change in temperature at the tip of a regulated device with electrical power around 4 mW at 2 Hz stimulation with increasing duty cycle (c) Infrared image of the bilateral device in hydrogel to simulate in vivo surroundings. Device outline is marked in black.

Supplementary Figure 11 Thermal Analysis

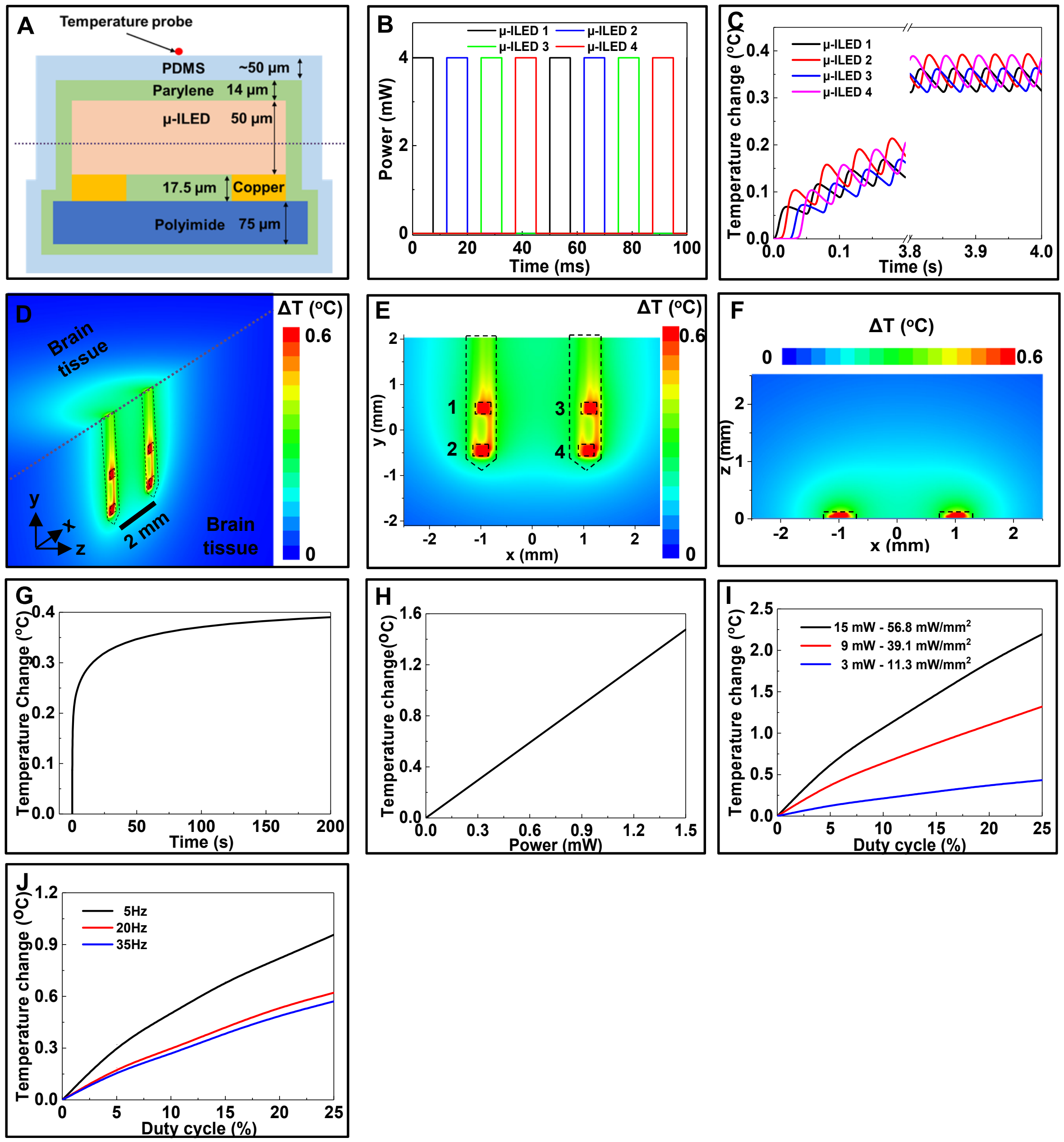

Supplementary Figure 11 Finite element analysis of the heating of brain tissue adjacent to a multi µ-ILED probe during various modes of operation (a) Cross-sectional schematic illustration of the model used for the simulations (lateral dimensions displayed in figure S1). The cross sectional cut is located at the center of one of the four µ-ILEDs of the system. The red dot indicates the spatial location of the temperature results presented in other frames of this figure. This position represents the location in the adjacent brain tissue that experiences the largest changes in temperature. (b) Plot of thermal power as a function of time for each of the µ-ILEDs during interlaced, pulsed mode operation, where the activation order is marked in panel (e). The peak values are 4 mW, which corresponds to an irradiance of 15.15 mW / mm^2 for each of the µ-ILEDs (c) Plot of the maximum change in temperature of the brain tissue as a function of time for operational conditions shown in frame (b). (d) 3D cutaway illustration of changes in temperature through the mid-line cross section of a probe, and adjacent brain tissue, for steady state operation at a continuous thermal input (0.4 mW per µ-ILED) that leads to increases in temperature that are comparable to those for the pulsed mode of frame (c) after a few seconds of operation. The position of the cutaway axis is indicated with a dotted line in the cross-sectional view in panel (a). (e), (f) Distribution of the change in temperature across the X-Y and Z-X planes. with operating conditions as in (d) (g) Change in temperature of the brain tissue as a function of time, evaluated at the position marked in panel (a) and with continuous thermal power from all four µ-ILEDs simultaneously (0.4 mW). (h) Change in temperature at this position as a function of continuous thermal power from all four µ-ILEDs simultaneously. (i) Average maximum change in temperature for pulsed operation at 20 Hz during operation in a mode illustrated in frame (b) as a function of thermal power. The corresponding irradiance values are in the legend. (j) Average maximum change in temperature for this same mode of operation as a function of frequency.

Supplementary Figure 12 MRI compatibility

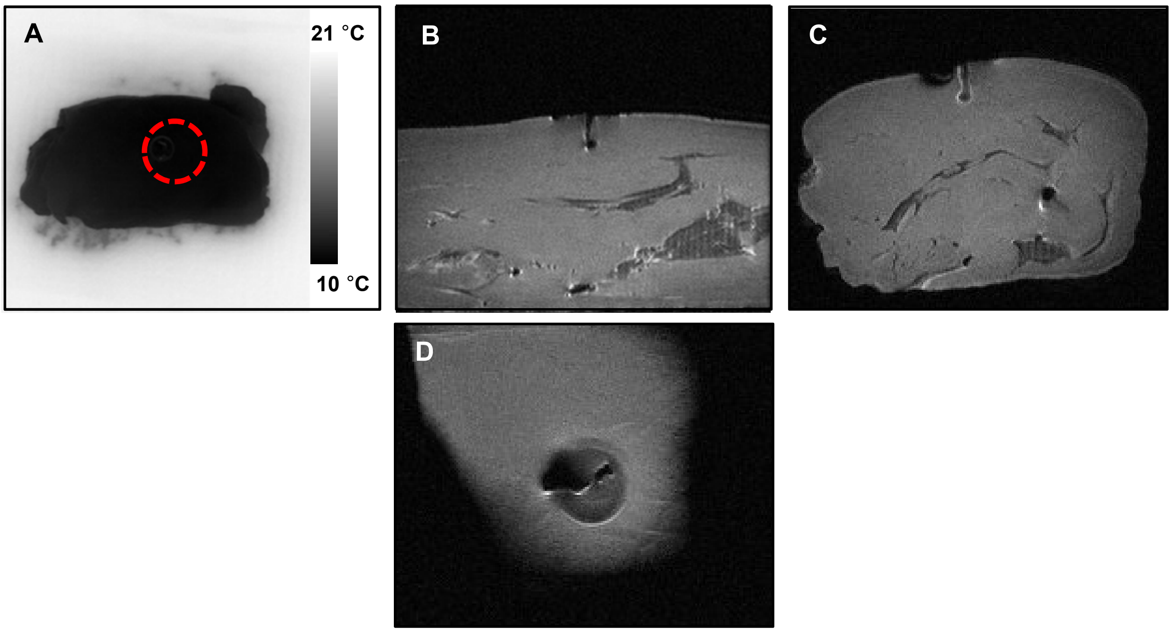

Supplementary Figure 12 Experiments to determine MRI safety of the implant. (A) Infrared camera image showing a chicken breast with implant after extensive imaging session. With no visible heating at the implant or in the tissue. MRI images of the chicken breast in (B) sagittal, (C) coronal and (D) axial orientation.

Supplementary Figure 13 Compatibility with imaging technologies – Subject 2

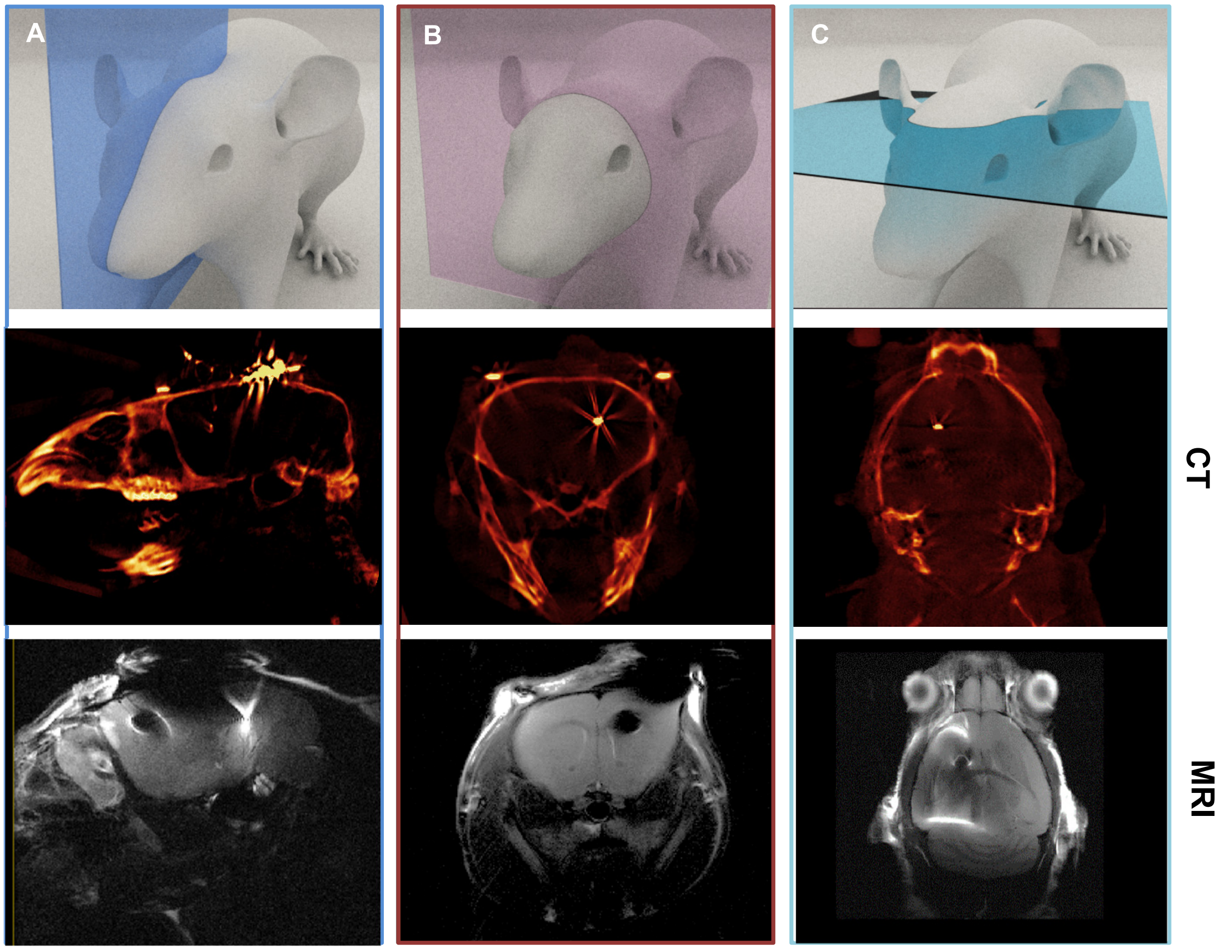

Supplementary Figure 13 MRI and CT imaging results of the constant intensity stimulation device (A) sagittal orientation, (B) axial and (C) coronal orientation.

Supplementary Figure 14 Compatibility with imaging technologies – Subject 3

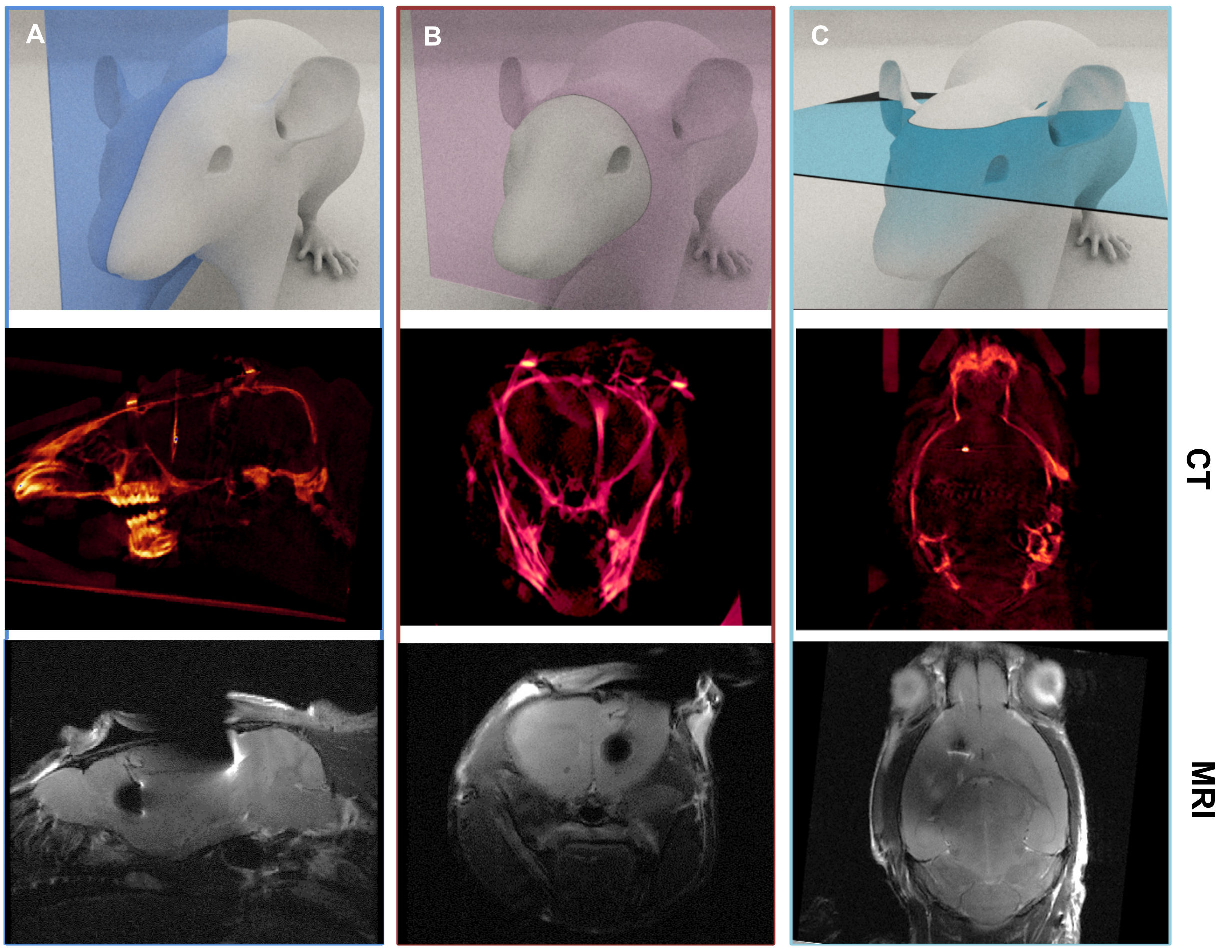

Supplementary Figure 14 MRI and CT imaging results of the constant intensity stimulation device (A) sagittal orientation, (B) axial and (C) coronal orientation.